Observation of intercalation-driven zone folding in quasi-free-standing graphene energy bands

Yi Lin,[1,*] Ge Chen,[1] Jerzy T. Sadowski,[2] Yunzhe Li,[1,†] Samuel A. Tenney,[2] Jerry I. Dadap,[1] Mark S. Hybertsen,[2] and Richard M. Osgood Jr.[1,‡]

[1]*Columbia University, New York, New York 10027, USA*

[2]*Center for Functional Nanomaterials, Brookhaven National Laboratory, Upton, New York 11973, USA*

(Received 18 June 2018; revised manuscript received 19 December 2018; published 22 January 2019)

Two-photon photoemission measurements reveal a near-zero-dispersion empty electronic state, approximately 2.6 eV above the Fermi energy and near the Brillouin zone center, induced by oxygen intercalation at the graphene-Ir(111) interface. While oxygen intercalation leads to quasi-free-standing graphene, electron diffraction shows 2×2 periodicity due to the patterned intercalant. Near the zone center, large-wave-vector zone folding, driven by this 2×2 periodicity, replicates states from near the Dirac cone that have little dispersion due to trigonal warping, explaining the nearly flat band. The zone-folding mechanism is supported by results from angle-resolved photoemission measurements and from density-functional-theory-based calculations of the unfolded energy bands. These results demonstrate zone-folding effects in graphene on a wave vector and energy scale that has largely been unexplored, and may open new opportunities to engineer the graphene electronic states.

DOI: 10.1103/PhysRevB.99.035428

I. INTRODUCTION

Recent advances in the ability to manipulate atomically thin, two-dimensional-material layers and stack them with multiple interfaces have enabled the discovery of a fascinating array of new condensed matter phenomena [1]. One important line of research has been the investigation of the impact of physical coupling between layers, to the supporting material, and the engineering of other structural perturbations to control the properties of electronic states. In fact, controlling the connection between periodic interfacial structure perturbations and the resulting changes in the electronic states remains fundamental to understanding a host of new phenomena in two-dimensional (2D) materials.

In the specific case of graphene, interaction with some substrates is so strong as to destroy the Dirac cones, a signature feature of the graphene band structure, e.g., Ni(111) [2], Ru(0001) [3], Co(0001) [4,5], and the initial (buffer) layer on SiC(0001) [6,7]. However, the interactions can be inherently weaker, such as for graphene on Ir(111) [8] and Pt(111) [9] or for the second layer of graphene on SiC [10,11] and Ru [3]. Control has been exerted by introducing intercalants such as noble metals at the interface with Ni(111) [2,12] and Ru(0001) [13], through the periodic potential induced by regular arrays of steps on the supporting metal [14–17] or SiC [18], by surface patterning with functional groups [19,20] or metal clusters [21], by intercalation of cations into graphene bilayers [22–24], and through the twist angle in bilayer graphene [25] or between graphene and other layers such as BN [26] or MoS_2 [27–29]. The essential features of the graphene band structure remain in these cases while the residual interactions perturb the graphene π states. In principle, control of those perturbations allows for active engineering of the Dirac fermion characteristics, including substantial renormalization of the velocity near the Fermi energy [30–33]. Examples include the opening of an energy gap at the Dirac point due to the breaking of the symmetry between the A and B sublattices [11–13], the appearance of energy-band replicas with "minigap formation" [3,8,10,17,27,34–36], and the induction of minibands in a magnetic field with a fractal spectrum (Hofstadter's butterfly) [37,38].

Most of these studies have focused on relatively long-wavelength perturbations of the graphene electronic states. Correspondingly, the replica bands have typically been displaced by a small wave vector in reciprocoal space and minigap formation has been studied only for a limited energy range near the Fermi energy. Much less studied have been shorter-wavelength, periodic perturbations and the impact on the graphene energy states over a wider energy range.

One fascinating exception has been studies of the intercalation of graphene bilayers by calcium [22] and by lithium [24]. An ordered structure was formed with a $\sqrt{3} \times \sqrt{3}R30^\circ$ periodicity. The electron donation from the intercalants resulted in high excess carrier concentrations. Angle-resolved photoemission spectroscopy (ARPES) studies showed evidence for large-wave-vector zone folding from the Brillouin zone corners to the zone center, following from that periodicity. Interestingly, there were similar, early observations for bulk graphite lithium intercalation compounds [39]. On the other hand, previous studies of the impact of oxygen and cesium intercalation at the Gr/Ir(111) interface did not reveal any impact on the graphene electronic states caused by periodic interface perturbations in the limited range of occupied π states probed in those experiments [35,36,40,41].

The goal of our work is to explore and understand band-folding effects that emerge when quasi-free-standing

*Corresponding author: yl3044@columbia.edu

†Present address: Boston University, Boston, MA 02215, USA.

‡Corresponding author: osgood@columbia.edu

graphene is created by oxygen intercalation at the Gr/Ir(111) interface. Due to the weaker interaction with the substrate, we expect the graphene electronic states to largely retain their identity. On the other hand, the graphene states are perturbed at a large characteristic wave vector associated with interaction between the graphene and the ordered oxygen intercalants. This is a regime that has not been previously explored.

Here, we report angle-resolved two-photon photoemission (AR-2PPE) measurements that reveal a near-zero-dispersion empty band near the zone center induced by the intercalation of oxygen. In addition, low-energy electron diffraction (LEED) measurements show that the dominant ordering pattern for the oxygen atoms is 2×2. For periodic perturbations with this spacing specifically, first-principles calculations demonstrate large-wave-vector band folding across the Brillouin zone. In particular, the nearly flat, empty band traces to the portion of the Dirac cone that is distorted by trigonal warping. The predicted impacts of zone folding at this length scale on the occupied states, particularly 6 to 8 eV below the Fermi energy, are further confirmed with ARPES measurements. Taken together, our results provide strong evidence for zone-folding effects in quasi-free-standing graphene at the wave vectors for the 2×2 ordering of the oxygen intercalants.

The primary perturbations to the graphene electronic structure found here are too far from the Fermi energy to influence low-field transport. However, further investigation of large-wave-vector perturbations to the graphene electronic states may well reveal impacts on high-field transport and other hot-carrier phenomena.

The balance of the paper is organized as follows. Experimental and theoretical methods are described in Sec. II. The main body of our results is presented and discussed in Sec. III. Section IV gives brief concluding remarks.

II. METHODS

A. Experimental methods

To synthesize quasi-free-standing graphene, we deposited graphene islands on a clean Ir(111) surface using cycles of temperature-programmed growth (TPG). The graphene coverage was approximately 67%. Partial coverage of graphene facilitated the subsequent intercalation process. Oxygen intercalation was accomplished by ramping the Gr/Ir sample to 550 K in a 5×10^{-6} Torr oxygen ambient to form an atomic oxygen intercalant sublattice [Gr/O(2×2)/Ir]. An O(2×2)/Ir surface was also prepared for ARPES measurements by treating a clean Ir(111) surface with the same process as was used for the oxygen intercalation. The sample preparation process was monitored via low-energy electron microscopy and spectroscopy (LEEM) in an aberration-corrected LEEM facility at the Center for Functional Nanomaterials at Brookhaven National Laboratory (BNL). The preparation method was reproduced at the x-ray photoemission electron microscopy (XPEEM) end station at the NSLS-II Electron Spectro-Microscopy (ESM) beamline at BNL and at Columbia University, for photoemission experiments.

Our AR-2PPE measurements were carried out at Columbia University with a high-repetition-rate femtosecond laser system [42]. The laser system made use of an ultrafast Ti:sapphire oscillator whose pulses were amplified in a regenerative amplifier and then used to drive an optical parametric amplifier to provide a tunable source of visible light. The visible output pulses were first frequency doubled in a β-BaB_2O_4 nonlinear crystal, which produced a train of tunable UV, sub-100-fs pulses, with photon energies in the 3.6–5.1 eV range at a 250-kHz repetition rate and a pulse energy of approximately 10 nJ in an estimated spot size of 200 μm. The 2PPE experiments for both Gr/Ir and Gr/O/Ir interfaces were conducted with laser light incident at 70° from the sample normal. The primary data set was acquired with p-polarized light, with selected additional experiments carried out with s-polarized light. Measurements were carried out at room temperature immediately following sample synthesis. The energy and momentum resolution of the spherical-sector energy analyzer are known from prior measurements to be 50 meV and 0.03 Å^{-1}.

The ARPES band structure maps were measured using the Elmitec XPEEM end station at the NSLS-II ESM beamline. The measurements were performed at room temperature in the XPEEM instrument by collecting spectra from micron-sized sample areas (μARPES). Soft x-ray radiation (energy $\hbar\omega = 55$ eV), incident at 73° from the sample normal, was used to excite photoelectrons, which were energy filtered by an imaging energy analyzer (energy resolution <0.25 eV), and whose angular distribution was mapped in reciprocal space using the electron optics and the detector system of the XPEEM. The raw data comprised photoelectron angular distributions beyond the first Brillouin zone (BZ) for energies from -12 to $+0.5$ eV relative to E_F, in increments of 0.1 eV. Projections along high-symmetry directions in reciprocal space were used to generate band structure maps along those directions.

B. Theoretical methods

Density functional theory (DFT) calculations were performed using the VASP suite with the projector augmented wave approach [43–45]. The atomic structure was determined including the role of van der Waals interactions explicitly (optB88-vdW exchange-correlation functional [46,47]). The in-plane lattice parameter was chosen to correspond to the calculated bulk Ir minimum energy lattice parameter ($a =$ 3.89 Å). The Gr/Ir(111) and Gr/O(2×2)/Ir(111) interfaces were modeled with a periodic slab consisting of four monolayers of Ir in an 8×8 supercell parallel to the interface. A 9×9 graphene supercell layer was matched to it. The graphene layer is correspondingly slightly compressed (1%). For the case of oxygen intercalation, one quarter of a monolayer with 2×2 periodicity was assumed with the oxygen atoms in the hcp hollow site, corresponding to previous studies of O/Ir surface phases [48,49]. The graphene and/or oxygen were placed on one side of the slab only. A minimum vacuum region of 25 Å was incorporated in the vertical direction of the supercell and dipole corrections were included [50].

All calculations were done with a basis determined by a 400-eV cutoff. The structure was determined in calculations performed with Γ-only sampling of the supercell Brillouin zone and a modest Gaussian broadening parameter in the sum

over states to determine the Fermi energy (0.1 eV). The top Ir layer, the O, and the graphene layer were relaxed to minimize the energy with a force criterion of 20 meV/Å. For evaluation of the electronic structure, self-consistency was redone with a 2×2 sampling of the Brillouin zone and a reduced broadening parameter (0.025 eV). The final electronic structure reported was calculated with a standard, gradient-corrected exchange-correlation functional (PBE [51]). Prior experience suggests that results for the energy bands will be a reliable guide in comparison to experiment, allowing for the known, modest underestimation of both the overall π band width and the Fermi velocity associated with the characteristic linear dispersion near the Dirac point due to limitations of using DFT-based energy bands [52,53].

To quantitatively assess the impact on the graphene π states due to interactions at the interface with Ir or O/Ir, the supercell energy bands were unfolded to the primitive Brillouin zone for graphene and represented as a spectral weight function. The unfolded bands show both the broadening of the graphene states and the introduction of replicas due to zone folding [54–56]. Specifically, the BANDUP code was used for the calculations [57,58] and the graphene π states were revealed by projection on the carbon atom p_z orbitals. For reference, a separate DFT calculation for a flat, isolated graphene layer was also performed in a 1×1 unit cell with the in-plane lattice parameter derived from the supercell. This calculation gave the expected, primary, and zone-folded energy bands for graphene. For presentation of the spectral weight versus energy at selected k points, Gaussian broadening was added with the half-width at half-maximum (HWHM) 0.3 eV chosen to approximate the peak widths observed in the measured ARPES energy distribution curves (EDCs).

III. RESULTS

A. Angle-resolved two-photon photoemission measurements

Figures 1(a) and 1(b) display the LEED patterns for Gr/Ir samples, prior to intercalation, and Gr/O/Ir samples, after intercalation. The diffraction patterns characterize the dominant periodic perturbation on graphene in the interface. For Gr/Ir, the dominant periodic perturbation is the moiré superstructure shown in Fig. 1(a). However, with oxygen intercalated, quasi-free-standing graphene is mainly perturbed by the 2×2 oxygen sublattice, indicated by the suppressed moiré pattern and the distinctive O(2×2) diffraction pattern in Fig. 1(b).

AR-2PPE was used to probe the unoccupied bands E_k at these interfaces with an energy range between the Fermi energy (E_F) and the vacuum energy (E_v) and with crystal momentum near the Brillouin zone center. Figures 1(c) and 1(d) display the 2PPE spectra and their second derivatives on the final-state energy scale relative to the Fermi energy for preintercalated Gr/Ir and intercalated Gr/O/Ir. This choice is common in the field, including recent studies of graphene and graphite [59–62]. For reference, the measured work function for each sample is added to the measured photoelectron kinetic energy. Specifically, the measured work functions for Gr/Ir and Gr/O/Ir samples with approximately 67% graphene coverage were 5.03 ± 0.02 and 5.54 ± 0.02 eV, respectively. We discussed the work functions for these samples elsewhere

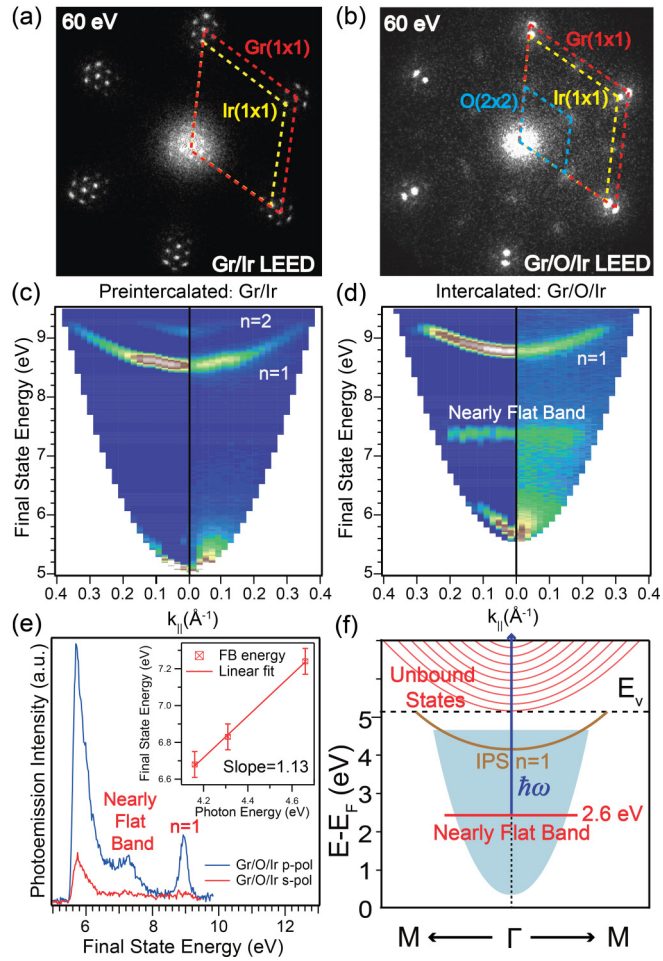

FIG. 1. LEED patterns of (a) Gr/Ir and (b) Gr/O/Ir. Iridium, graphene, and oxygen sublattices are highlighted by a dashed rhombus in yellow, red, and blue, respectively. AR-2PPE spectra (panel right) and their second derivatives with respect to energy (panel left) using the final-state energy scale ($\hbar\omega = 4.66$ eV) for (c) preintercalated Gr/Ir, (d) intercalated Gr/O/Ir along Γ-M. (e) Energy distribution curve at the Γ point for p- and s-polarized incident photons for Gr/O/Ir. Inset: final-state energy of the nearly flat band identified in (d) versus incident photon energy with a linear fit. (f) Energy diagram illustrating intermediate states probed by the second photon excitation, particularly the nearly flat band, in Gr/O/Ir with energy referred to the Fermi energy. The shaded areas present the momentum space accessible in our 2PPE experiments.

in detail [63]. The values can be seen as the onset of the allowed energy-momentum region on the final-state energy scale in Figs. 1(c) and 1(d).

For the case of preintercalated Gr/Ir, the major features in Fig. 1(c) are the well-known image potential states observed in the 8.5 to 9.5 eV energy range [63,64], along with the usual broad feature reflecting secondary electrons in the 5 to 6 eV energy range at the bottom of the spectrum. Upon oxygen intercalation, as shown in Fig. 1(d), a single image potential band is observed starting at about 8.8 eV [63], as well as broad features, again reflecting secondary electrons, in the 5.5 to 6.5 eV range. However, there is an additional band observed in Fig. 1(d) at 7.3 eV on the final-state energy scale. The new

feature is essentially flat, with dispersion estimated to be no more than 0.05 eV in the scope of wave vector measured. This is in contrast to the clear dispersion exhibited by the image potential band. Significantly, such a nearly flat band was not observed in AR-2PPE measurements on a deintercalated Gr/Ir interface.

To further investigate the nature of this previously unobserved nearly flat band, we varied the polarization and photon energy of the incident laser. The energy distribution curves at the Γ point are shown in Fig. 1(e). When the laser polarization is switched from p polarization to s polarizaton, the peaks associated with the image potential state at 9 eV and with the nearly flat band identified here at 7.3 eV are both suppressed.

This selection rule for the image potential state is consistent with specific, previous measurements on graphite surfaces [62,65]. It is also consistent with the basic physical picture for dipole-allowed transitions in ARPES. For s-polarized light with the electric vector perpendicular to the plane of detection, defined by the orientations of the incident light and the detected photoelectron, excitation from states that have even parity with respect to that plane is forbidden. As discussed previously, this suppression for s-polarized light applies to emission from electrons excited into π^* bands [62,65] and other surface electronic states such as observed in the Gr/Cu(111) system [66]. Thus, the results in Fig. 1(e) suggest that the nearly flat band is either related to graphene π^* states or to some other surface-localized states made up of orbitals consistent with the restriction to even parity relative to the detection plane, e.g., oxygen p_z orbitals.

The incident photon energy dependence is shown in the inset of Fig. 1(e). The energy of the nearly flat band scales linearly with the incident photon energy. This specifically indicates that the signal originates from an intermediate state in the energy gap. Therefore, by subtracting one photon energy (e.g., 4.66 eV) from the final-state scale, the energy of the nearly flat band is measured to be 2.6±0.1 eV above the Fermi level as illustrated in Fig. 1(f).

B. Electronic structure calculations

The model atomic structures used in the DFT calculations for the Gr/Ir(111) and Gr/O(2 × 2)/Ir(111) interfaces are illustrated in Figs. 2(a) and 2(b), respectively, showing the top view. The final, relaxed structures agree with prior results. Specifically, for the Gr/Ir(111) interface, corrugation of the graphene emerged with an amplitude of about 0.33 Å and the average distance from the Ir surface layer and the graphene layer was 3.55 Å. The average distance of the Ir surface layer from the frozen layer below was reduced by 0.02 Å from the bulk value. Prior DFT calculations, reported for a model structure that was Gr(10 × 10)/Ir(9 × 9) and based on the DFT-D approach to include van der Waals interactions, resulted in a corrugation of 0.35 Å and an average height of 3.41 Å [67]. Another DFT calculation, reported using the same model structure and exchange-correlation functional as in this work, resulted in a corrugation of 0.38 Å and an height of 3.53 Å [36].

In the presence of one quarter of a ML of oxygen, the corrugation of the graphene was reduced to 0.16 Å and the average distance from the Ir surface layers was increased to

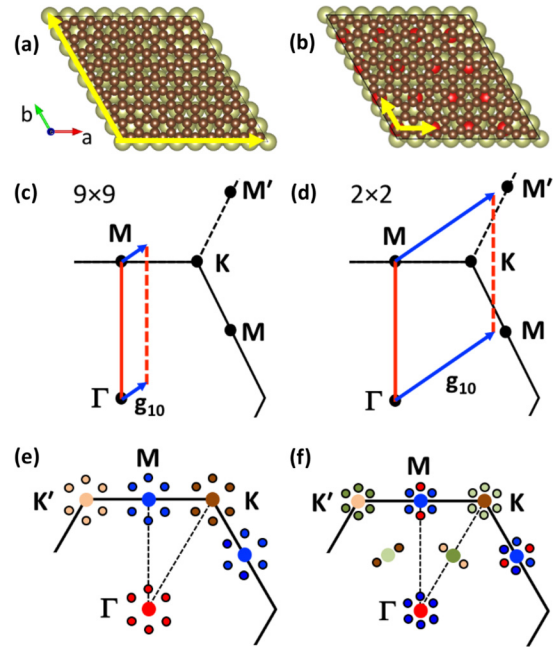

FIG. 2. Supercells used for calculations: (a) Gr(9×9)/Ir(8×8) and (b) Gr(9×9)/O(2×2)/Ir(8×8). Yellow arrows denote the dominant periodicity. Illustration of representative replicas from zone folding for the Γ-M line for (c) Gr/Ir and (d) Gr/O(2×2)/Ir in the 1 × 1 graphene Brillouin zone. (e), (f) Color coded maps in the graphene Brillouin zone illustrating selected replicas induced by band folding by the stars of vectors illustrated in (c) and (d) and corresponding to the Gr/Ir and Gr/O(2 × 2)/Ir cases, respectively. Γ-K and Γ-K' lines are not formally equivalent and highlighted points are distinguished by light and dark shades. K' folds to close to the midpoint of the Γ-K line.

3.95 Å. For comparison, the prior study with the same method reported 0.14 Å corrugation and 4.02 Å average height [36]. The average oxygen to surface Ir distance was 1.21 Å and the average surface Ir layer relative to the subsurface Ir layer was increased by 0.03 Å compared to bulk. Naturally, the surface Ir atoms also responded to the surface oxygen both laterally and vertically on a scale of about 0.1 Å. The presence of the graphene layer pushed the oxygen atoms about 0.1 Å closer to the Ir surface. In the absence of graphene, we found the oxygen atoms to be 1.32 Å above the average Ir height, in agreement with prior calculations [48,49].

The interaction of the graphene with the substrate in each case will result in perturbations to the graphene π states. Focusing on the dominant wavelength for scattering, Figs. 2(c) and 2(d) illustrate features of the models in reciprocal space relative to a segment of the Brillouin zone for graphene. In the reference Gr/Ir(111) case, the overall formation of the moiré pattern, including the corrugation of the graphene layer, sets the spatial scale [yellow arrows in Fig. 2(a)] and the corresponding wave-vector scale [blue arrows in Fig. 2(c)]. For the Gr/O(2 × 2)/Ir(111) intercalated system, the dominant wavelength corresponds to the lateral surface oxygen separation [yellow arrows in Fig. 2(b)] and a four-times larger wave vector in reciprocal space for our model supercells [blue arrows in Fig. 2(d)]. Overall, the interface-induced potential

perturbation will mix states along the Γ-M line, for example, with those displaced by $\mathbf{g_{10}}$ and five other supercell reciprocal lattice vectors of the same length. A zeroth-order picture is that energy bands $E_n(\mathbf{k}+\mathbf{g_i})$ will appear as replicas at $\mathbf{k}$, further modified by the interactions. As the comparison of Figs. 2(c) and 2(d) makes clear, the difference in magnitude of the respective wave vectors $\mathbf{g_{10}}$ results in replicas along the Γ-M line from close-by states in the Gr/Ir(111) case and from the M-K'-M region in the Gr/O(2 × 2)/Ir(111) case, a substantial difference.

An alternative illustration of the impact of zone folding for each model is shown in Figs. 2(e) and 2(f). A few high-symmetry points in the graphene Brillouin zone are highlighted and color coded. In the case of Gr/Ir(111) with a large periodicity and correspondingly short-wave-vector perturbation, satellite points around each one illustrate replicas that derive from the *same* point in the Brillouin zone [Fig. 2(e)]. So, for instance, near the K point the electronic states near the Dirac cone will be mixed with six replicas of the Dirac cone nearby [8,68]. In contrast, for the case of Gr/O(2 × 2)/Ir(111) with a larger-wave-vector perturbation, the satellite points derive from further away. In particular, the electronic states near the Γ point will interact with replicas that derive from six M points around the hexagonal Brillouin zone. On the other hand, the M point will interact with replicas deriving both from the Γ point and from other M points, including some from an extended zone scheme not shown in Fig. 2(f). This sets up a reciprocal relationship between the regions near the Γ and M points that should be evident in spectral functions due to zone folding. Similarly, as indicated in Fig. 2(f), the K point is surrounded by replicas from near the midpoint along the Γ-K' line and vice versa.

The unfolded spectral weight for the graphene π states for the Gr/Ir(111) and Gr/O(2×2)/Ir(111) cases are shown in Figs. 3(a) and 3(b), respectively, from the full DFT calculations. A magnification along the chosen line segment near the K point is shown in Fig. 3(c). The electronic states are studied along selected high-symmetry lines in the graphene BZ (M-Γ-K-M') as illustrated in Fig. 3(d). The expected graphene bands are clearly visible. However, they are perturbed and new states appear. In the case of Gr/Ir(111), the region near the Dirac point at K shows characteristic crossings by replica bands and minigap formation, as seen in Fig. 3(c). The spectral weights for the Gr/O(2 × 2)/Ir(111) case shown in Fig. 3(b) are quite different. In particular, empty states with near-zero dispersion appear near Γ at around 2.5 eV above the Fermi level.

To illustrate the main effects of band folding in each case, we also show in Figs. 3(a)–3(c) the superposed energy bands for free-standing graphene (solid lines) and the zeroth-order folded bands according to the dominant star of reciprocal lattice vectors illustrated in Figs. 2(c) and 2(d) (dashed lines), from an equivalent DFT calculation. They have been shifted in energy to align the Dirac point to the p-doped scenario in each case. The excellent agreement between the superposed bands and spectral weights confirms the basic zone-folding picture to account for the interface perturbed π states in Gr/Ir and Gr/O(2 × 2)/Ir(111).

Focusing on the impact near the Dirac point in the reference Gr/Ir(111) case, we find that there are several band crossings between replica and primary bands. One can think of the replica bands (each doubly degenerate) that have maxima (minima) around −1 eV (+1 eV) as deriving from the Dirac cones around the four replicas of the K point that are closest to the Γ-K-M' line, following the illustration in Fig. 2(e). The two replicas that are further away (perpendicular distance) give rise to the replica band (doubly degenerate) that has a maximum (minimum) around −1.5 eV (+1.5 eV, not shown). The position of the maximum is displaced from K due to trigonal warping. Together, these replica bands give rise to mini-band-gap formation. In the occupied states, the two crossings near −1 eV result in gaps whose magnitudes are in agreement with previously published, high-resolution ARPES measurements [8,68].

The calculated energy band structure also shows relatively flat bands that appear near the Fermi energy and interact with the graphene π bands near the Dirac point. These result in additional minigap formation. Further analysis shows that they derive from coupling to surface Ir dz^2 states. As a consequence, near the Fermi energy in Fig. 3(c), the graphene band shape is distorted from linear and shows a weak maximum. The ARPES measurements also show some evidence of distortion, but the resolution limits the distinction of the details seen in the present calculations [8]. In comparison with Fig. 3(b), this additional flat feature is suppressed upon oxygen intercalation. More broadly, the chosen model structure, with the relaxed structure found with DFT, gives rise to potential perturbations in the graphene layer that reproduce the main features found in the ARPES measurements, validating our approach.

Turning to the impact of oxygen intercalation, we observe that the replica bands are completely different, due to the much larger wave vector associated with the dominant O(2 × 2) length scale and anticipated in the discussion of Fig. 2. In particular, we observe several distinctive features such as a confluence of folded bands near −3 eV around the Γ point of the Brillouin zone and near −5 eV near the K point. The nearly flat band along the M-Γ line is also naturally explained.

To illustrate specifically the emergence of the nearly flat band as a consequence of zone folding induced by the perturbation from the intercalants, Fig. 3(e) shows the free-standing graphene electronic structure shifted in energy to align the Dirac point to the p-doped scenario in Fig. 3(b). We plot the empty π-state dispersion in an extended zone scheme. The reference lines from the graphene Brillouin zone and the line that contributes to the zone-folded nearly flat band are shown with the contour plot of the energy band.

The three-dimensional representation has been cut to highlight the origin of the nearly flat band. Specifically, the cut [red shaded plane in Fig. 3(e)] passes through a portion of the Dirac cone that is distorted by trigonal warping, leading to the nearly flat empty band (red curve) folded back to the zone center and observed in our AR-2PPE experiment. The argument is made here for the 2 × 2 oxygen structure. However, it equally well applies to a mixture of 2 × 1 oxygen structures where all three angular orientations appear. Quantitatively, the calculated dispersion of the free-standing graphene band that is folded back is 0.16 eV, reflected in the dashed line in Fig. 3(b). Only a portion of the folded band is visible in the scope of the AR-2PPE data in Fig. 1(d) and the impact

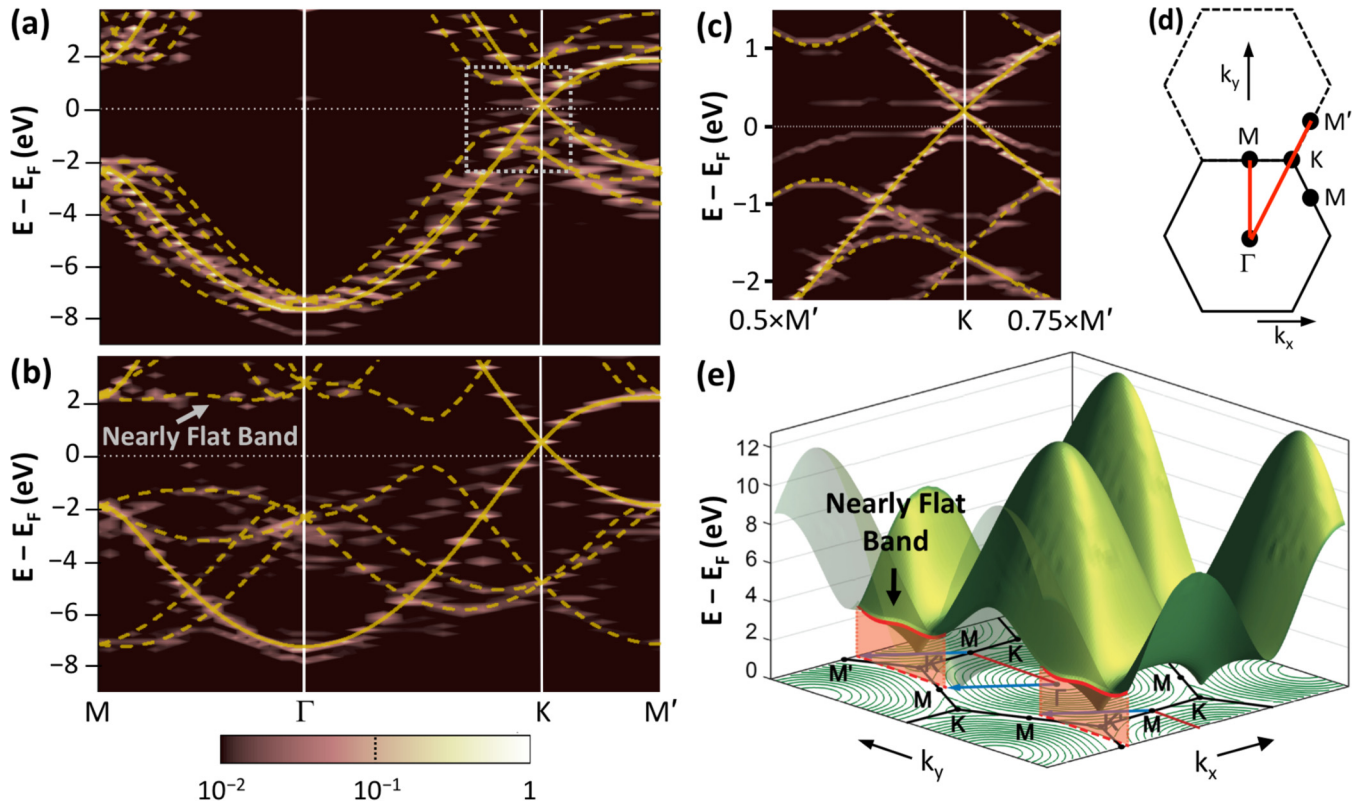

FIG. 3. Calculated spectral weights showing the unfolded, graphene π-state band structure for (a) Gr/Ir and (b) Gr/O(2×2)/Ir in false color on a logarithmic scale. (c) Magnification of the calculated spectral weight within the dashed white rectangle area in (a). In (a), (b), and (c), superposed lines show the pure graphene π-state bands $E_n(\mathbf{k})$ (solid lines) and the replicas induced by zone folding from the star of superlattice reciprocal lattice vectors $E_n(\mathbf{k}+\mathbf{g}_i)$, as illustrated in Figs. 2(c) and 2(d), respectively (dashed lines). (d) Brillouin zones of graphene primitive cell with red lines indicating the path along which electronic states were calculated. (e) Calculated pure graphene π^* band, shifted in energy to align the Dirac point to the p-doped scenario in (b), also represented by constant energy contours (green curves) with Brillouin zone designations (black lines). A cut through the energy band is highlighted in red, corresponding to representative regions that are replicated by zone folding in Fig. 2(d), resulting in the band with near-zero dispersion.

of interactions with the substrate seem to further flatten the dispersion near Γ in the full DFT calculations in Fig. 3(b).

To provide a more quantitative estimate of the relative intensities of the zone-folded spectral features, we show the calculated spectral weight distributions in energy at selected symmetry points for the Gr/Ir(111) and Gr/O(2×2)/Ir(111) cases in Figs. 4(a)–4(d). Guided by the illustration of replicas shown in Fig. 2(f), we have chosen pairs of points that are approximately linked by a fundamental zone-folding wave vector in the Gr/O(2×2)/Ir(111) case. The main π-state features near +2 and −2 eV at the M point [Fig. 4(a)] are echoed by peaks at similar energies at the Γ point, highlighted by blue arrows [Fig. 4(b)]. The energy alignment is not exact because, as shown in Fig. 2(f), the M-point replicas are close to Γ and dispersion affects the energy position of the states exactly replicated at Γ. Correspondingly, the strong π state near −7.5 eV at Γ [Fig. 4(b)] is replicated at M, as indicated by the red arrow [Fig. 4(a)].

Similarly, the primary π-state feature near −5.5 eV at 0.5(Γ-K) [Fig. 4(c)] leads to a clear replica in the spectral weight at the K point, denoted by a green arrow in Fig. 4(d). In the complementary direction, the π states near the Dirac point create faint replicas near the Γ-K line, denoted by the orange arrows in Fig. 4(c). In this case, the strong dispersion near the Dirac point leads to a more significant energy shift. In fact the, zone-folding effect in this case is more easily seen in the original band-structure-like presentation in Fig. 3(b). The dashed lines highlight the folded bands near the Fermi energy that are the result of cuts through the Dirac cones centered at the two replica points that straddle the Γ-K line [Fig. 2(f)], although the calculated spectral weight is rather weak.

Comparing the spectral weight at these four high-symmetry points between the Gr/Ir(111) and Gr/O(2×2)/Ir(111) cases in Fig. 4, we find that several further points emerge. First, the degree of effective p doping is different between the two cases, so there is a small shift in energy of the main π states. Specifically, the Gr/Ir(111) π states are about 0.4 eV deeper. Second, the interactions between the graphene and the metal support differ, so the extent of electronic coupling to the states in the metal support varies and, correspondingly, the spectral distribution in energy can be seen to differ. But, finally, and most importantly, the replicas that are easily explained by zone folding in the Gr/O(2×2)/Ir(111) case are not seen in the Gr/Ir(111) case. These replicas are specifically due to the 2×2 intercalated oxygen at the interface.

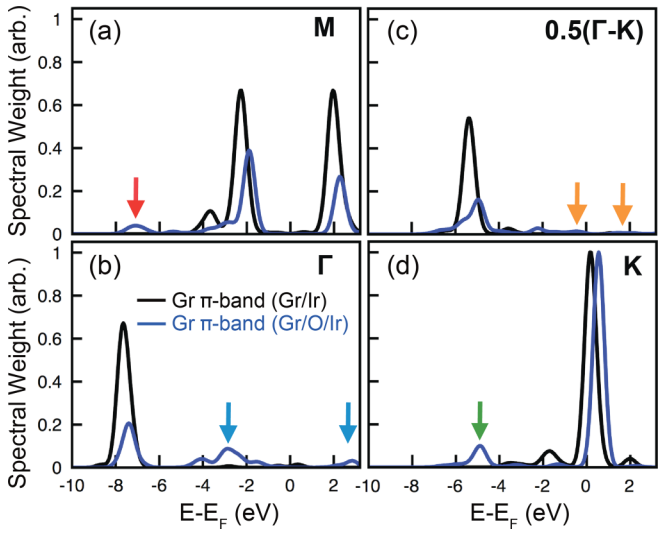

FIG. 4. (a)–(d) Calculated spectral weight versus energy with Gaussian broadening (0.3 eV HWHM) for the graphene π band in Gr/Ir(111) (black) and Gr/O(2 × 2)/Ir(111) (blue) at selected points in the graphene Brillouin zone: (a) M point, (b) Γ point, (c) halfway along Γ-K, and (d) K point. Arrows, color coded to indicate the origin of the zone-folding following Fig. 2(f), highlight extra spectral intensities due to zone-folding effects in the 2 × 2 oxygen intercalated case.

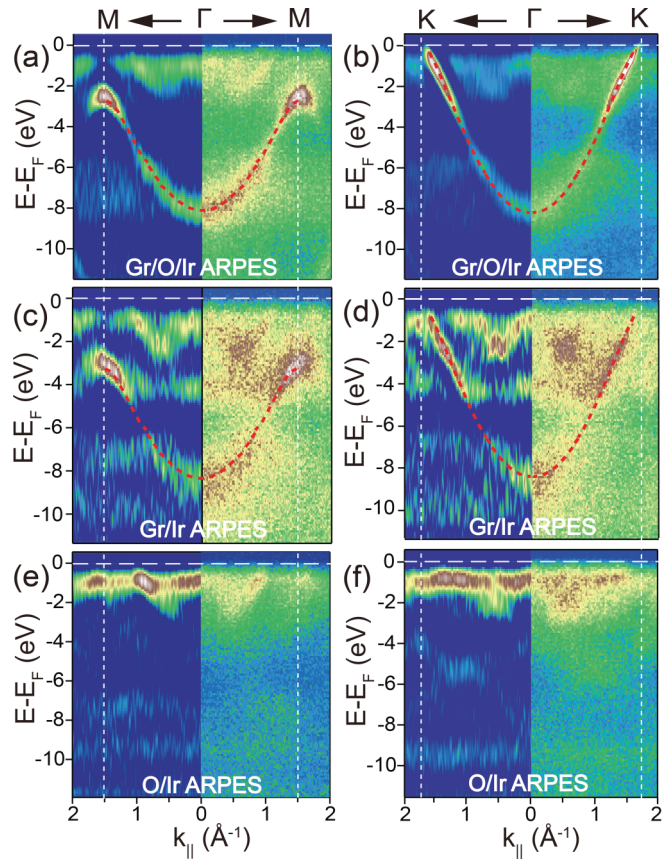

FIG. 5. (a)–(f) ARPES spectra of Gr/O/Ir, Gr/Ir, and O/Ir samples along the Γ-M and Γ-K directions. Each panel shows a false color map of raw data (right) and the second derivative with respect to energy (left). Red dashed lines show the calculated π bands of free-standing graphene.

C. Angle-resolved photoemission measurements

In order to further probe the impact of the band folding, we carried out ARPES measurements of the occupied band structure. As noted in Sec. II, the Gr/O/Ir sample has approximately 67% coverage of graphene, which leaves exposed O/Ir elsewhere. To distinguish the signal specifically from the quasi-free-standing graphene, we measured an independent O/Ir sample with similar oxygen coverage and order for reference. For comparison, we also measured an unintercalated Gr/Ir sample. These measurements were made consecutively at the same ARPES facility and with a consistent set of data-acquisition parameters. Band structure maps $E(k_x, k_y)$ were obtained at room temperature *in situ* in the XPEEM from micron-sized sample areas. The light source is highly p polarized so that contributions from σ bands are negligible.

Figures 5(a)–5(f) display the 2D ARPES maps for the three interface cases. The primary, dispersive band due to the occupied graphene π states is clearly visible for both the Gr/O/Ir and Gr/Ir cases. The band is more distinct, with stronger spectral intensity in some energy ranges and in some areas of reciprocal space. In particular, there is a dip in the intensity in the −6 to −4 eV range. In the Gr/Ir data, there are other visible spectral features, particularly in the regions between −2 eV and the Fermi energy, and around −4 eV. These are due to Ir metal d states, based on previous ARPES measurements for bare Ir(111) and Gr/Ir [68,69]. Details of the dispersion of these states are not resolved here based on the present ARPES resolution and measurements performed at room temperature. The spectral weight in these energy regions changes upon oxygen intercalation, so that the spectral weights outside the scope of the graphene π states in Figs. 5(a) and 5(b) are much closer in character to those found for O/Ir [Figs. 5(e) and 5(f)]. In the O/Ir case, most of the signal is between −2 eV and the Fermi energy, indicative of the impact of oxygen on the Ir surface states and likely mostly due to O p_z states.

To understand whether signatures of the zone-folding emerge along the lines suggested by theory, we present the measured ARPES energy distribution curves (EDCs) at the same four high-symmetry points in Figs. 6(a)–6(d). Starting with the M point, a clear feature near −2 eV is seen in both the Gr/O/Ir and Gr/Ir EDCs in Fig. 6(a), the expected position of the π band. By contrast, the O/Ir EDC only exhibits a broad, rising intensity between −4 eV and the Fermi energy.

The π band for the Gr/Ir case is deeper bound by 0.56 eV. Thus, we find that the graphene layer in the Gr/O/Ir case is effectively more p doped than that in Gr/Ir, in very good agreement with two prior reports based on ARPES measurements, specifically 0.57 [35] and 0.58 eV [41]. Another study found a larger shift, about 0.73 eV, suggested to be due to a higher coverage of intercalated oxygen [36]. The shift is slightly larger than that found in our DFT calculations, possibly due to an intercalated oxygen concentration slightly above the assumed quarter of a monolayer.

Turning to the Γ point EDCs shown in Fig. 6(b), we observe the π band near −8 eV in both the Gr/O/Ir and Gr/Ir

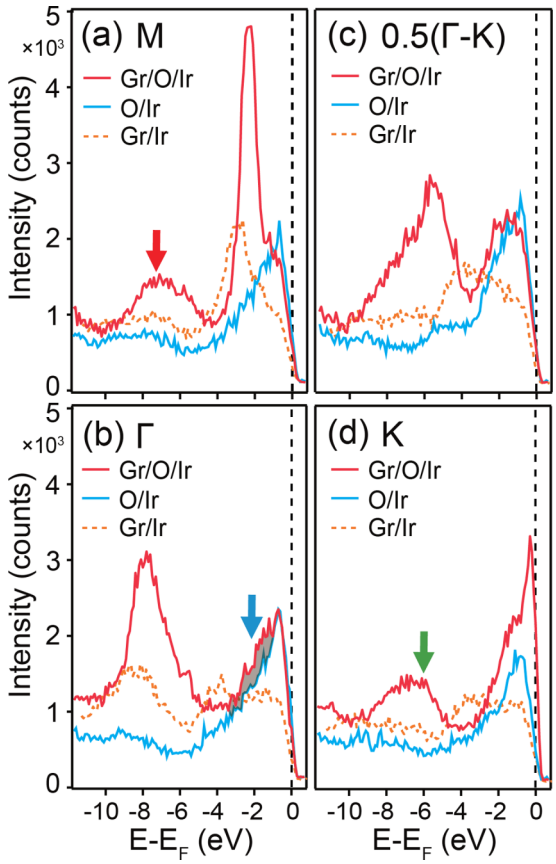

FIG. 6. (a)–(d) ARPES energy distribution curves (EDCs) for Gr/O/Ir, O/Ir, and Gr/Ir samples at selected points in the graphene Brillouin zone: (a) M point, (b) Γ point, (c) halfway along Γ-K, and (d) K point. Arrows indicate the extra spectral intensities predicted due to zone-folding effects induced by a 2×2 potential perturbation.

data, with a shift similar to that observed at the M point. The EDC for Gr/O/Ir at the midway point along Γ-K shows a clear peak attributable to the π band near -6 eV in Fig. 6(c). On the other hand, the EDC for Gr/Ir shows no significant intensity above background in this range. With reference to the full data set in Fig. 5(d) where the full dispersion of the π band can be tracked, there is minimal intensity in that region of energy and reciprocal space, as noted above. Finally, the EDC at the K point for Gr/O/Ir shows rising intensity approaching the Fermi energy, consistent with the linear dispersion for the π band seen in the full data set in Fig. 5(b). For the Gr/Ir case, the intensity near the Fermi energy in Fig. 5(d) drops off and the π band is not resolvable right at the K point.

Now, following the logic of the zone folding illustrated in Fig. 2(f), the Γ point π band near -8 eV corresponds well with a clear additional spectral feature seen in the Gr/O/Ir EDC at the M point in the -8 to -6 eV range, highlighted by the red arrow in Fig. 6(a). By contrast, the EDCs for Gr/Ir and O/Ir do not show a similar feature. The reciprocal zone-folding relationship, namely, the signature for a replica of the π band near -2 eV, is only weakly discerned in the EDC at the Γ point. The rising background coming from the O/Ir obscures other contributions. The EDCs for Gr/O/Ir and O/Ir do match relatively well for the maximum in the intensity near -0.5 eV. Then, at deeper energy, there is some extra intensity in the Gr/O/Ir EDC. This feature is consistent with a replica from near the M point, but not particularly conclusive by itself. Turning to the K point, there is a clear extra peak in the Gr/O/Ir EDC in the -8 to -6 eV range. This peak aligns with the π band from midway along the Γ-K line shown in Fig. 6(c). Also, that feature is not seen in the EDCs for either Gr/Ir or O/Ir. Finally, any possible evidence along the Γ-K line for a replica coming from the Dirac cone and appearing between -2 eV and the Fermi energy is obscured by the strong, rising background in that energy range.

To summarize the implications of the ARPES data, we have identified extra features at both M and K in the -8 to -6 eV range that only appear in the Gr/O/Ir sample. These are fully consistent with being replicas created by the 2×2 ordering-induced wave vector.

IV. DISCUSSION AND CONCLUSION

The process of intercalating oxygen at the Gr/Ir interface created a quasi-free-standing graphene layer. Interactions between the graphene and the substrate were reduced. The LEED measurements showed a reduced intensity for the satellite diffraction peaks attributable to the Gr/Ir moiré and the emergence of a 2×2 periodicity attributable to the intercalated oxygen. Our AR-2PPE measurements revealed a new empty band about 2.6 eV above the Fermi energy and near the center of the Brillouin zone, specifically caused by the oxygen intercalation. The low background and good sensitivity to intermediate states in the energy range between the Fermi energy and the vacuum level of the AR-2PPE technique facilitated this measurement.

In seeking to understand the origin of this new electronic feature, we have used DFT-based calculations to examine whether residual interactions between the quasi-free-standing graphene and the O/Ir supporting surface could be responsible. While zone folding has been extensively explored for graphene weakly perturbed by a variety of physical mechanisms, the effects caused by perturbations at the wave vectors associated with 2×2 periodicity had not been investigated. Our calculations reproduced replica and minigap formation previously observed for Gr/Ir(111). Further, the calculations for the Gr/O(2×2)/Ir(111) case showed clear evidence in the electronic states for extra spectral weight due to zone folding. In particular, the emergence of a nearly flat, empty band near the center of the Brillouin zone and extending across the zone was naturally explained. The wave vectors associated with 2×2 periodicity fold a region of the graphene energy band structure near the zone edge that is strongly affected by trigonal warping to overlap with the center of the graphene Brillouin zone.

The DFT calculations suggest that a similar effect occurs in the occupied π bands, although that folded band exhibits more dispersion. Graphene energy bands are not specifically symmetric between the π and π^* bands at this energy scale. Signatures of zone folding deeper in the occupied bands were also identified. We performed ARPES measurements, carried out over a broad energy range, to map the full π-band dispersion in the occupied states. Unfortunately, relative high backgrounds in the ARPES data obscured a clear signature

associated with a zone-folded band in the range of −3 to −2 eV below the Fermi energy. Only a weak feature could be identified by focusing on the EDC at the Γ point in this energy range. However, looking deeper into the π bands, we identified clear replica signatures in the EDCs at the M and K points of the Brillouin zone.

The root of our study is the AR-2PPE measurement that revealed the nearly flat, empty state. We have considered other possible sources of the observed nearly flat band. One possible origin could be related to the oxygen layer itself. However, based on the DFT calculations for the Gr/O(2×2)/Ir(111) model structure, analysis of the spectral weight associated with the oxygen p_z orbitals did not show a signature consistent with the observed empty state. In particular, oxygen p_z spectral weight at the Γ point was much less intense as compared to the carbon p_z spectral weight and centered near 1 eV, too close to the Fermi energy. Another possibility is that extra oxygen atoms within the 2×2 structure, or other structural variation in the oxygen coverage, give rise to a defect band. We did not test this case with further computations, but we suggest that it is unlikely that such a defect-derived oxygen p_z spectral weight could account for both the observed empty band *and* the extra features seen in the ARPES data in the −8 to −6 eV range, including the dispersion. Furthermore, the extra features in the −8 to −6 eV range were not observed in the ARPES results for the O/Ir sample.

Another consideration is whether a physical mechanism other than the interaction with the ordered oxygen intercalants could be the cause. In the case of bulk graphite, AR-2PPE studies showed evidence for intermediate state occupancy of π^* from the high density of states saddle point at M [65,70,71]. Weak, nondispersive features have also appeared in ARPES [72,73] and inverse photoemission [74,75] at energies that would similarly correspond to M-point derived states. These observations have generally been attributed to indirect transitions, assisted by scattering mechanisms that were not clearly established.

Electron-phonon scattering is an intrinsic mechanism. For graphene, it has an established role in scanning tunneling spectroscopy [76] and indirect ARPES signals near Γ [77,78], both confirmed by the appearance of gaps at low bias or energy. Detailed calculations support this picture, but suggest an upper bound of 2% on the spectral weight induced near Γ by electron-phonon scattering from near the K and K' points [79]. By comparison, we calculate spectral weight for the zone-folded π^* bands induced near Γ by the ordered oxygen intercalants to be ∼10%, five times larger than the upper bound estimated for electron-phonon scattering. In our AR-2PPE studies for both preintercalated Gr/Ir and deintercalated Gr/Ir, we find no features corresponding to the M-point π^* bands, in agreement with other studies for Gr/Ir [61,64,80]. The lack of observed features places an upper bound on the role of the intrinsic electron-phonon mechanism to induce π^*-related peaks in 2PPE. Under our measurement conditions, we estimate that such a feature could be at most 10% of the signal we measure due to oxygen intercalation. Clearly, the intercalant effects dominate.

To conclude, we have investigated the manipulation of quasi-free-standing graphene electronic energy bands by zone folding in a regime that has not been previously studied. The specific wave vector of the perturbation created by oxygen intercalation led to previously unexpected features, including a signature of the π^* bands near the zone center about 2.6 eV above the Fermi energy. Perturbations with these relatively large wave vectors still remain largely unexplored.

This method to alter the interface electronic structure may well extend to other intercalation species, with the possibility to tune the interaction strength and to manipulate the interface ordering. The latter in particular could result in additional control of the wave vector leading to alternative zone-folding results. In the example we have discovered, the strongest signatures of the band folding occur 2–3 eV away from the Fermi energy. With further investigation, stronger zone-folding effects may be identified for electronic states closer to the Fermi energy. Of course, the proximity of the manipulated energy bands to the Fermi energy, considering a scope of plausible doping, affects their impact on low-field transport. However, under conditions of high-field transport or optical excitation, changes to empty or occupied energy bands further from the Fermi energy could affect the distribution of hot carriers through the Brillouin zone and their dynamics.

ACKNOWLEDGMENTS

R.M.O. and Y.L. acknowledge support from the U. S. Department of Energy, Office of Basic Energy Sciences, under Contract No. DE-FG02-90ER14104. Our research used resources of the Center for Functional Nanomaterials and the National Synchrotron Light Source II, which are U. S. DOE Office of Science Facilities, and the Scientific Data and Computing Center, a component of the Computational Science Initiative, at Brookhaven National Laboratory, under Contract No. DE-SC0012704.

[1] A. K. Geim and I. V. Grigorieva, Nature (London) **499**, 419 (2013).

[2] A. Varykhalov, J. Sanchez-Barriga, A. M. Shikin, C. Biswas, E. Vescovo, A. Rybkin, D. Marchenko, and O. Rader, Phys. Rev. Lett. **101**, 157601 (2008).

[3] P. Sutter, M. S. Hybertsen, J. T. Sadowski, and E. Sutter, Nano Lett. **9**, 2654 (2009).

[4] A. Varykhalov and O. Rader, Phys. Rev. B **80**, 035437 (2009).

[5] D. Eom, D. Prezzi, K. T. Rim, H. Zhou, M. Lefenfeld, S. Xiao, C. Nuckolls, M. S. Hybertsen, T. F. Heinz, and G. W. Flynn, Nano Lett. **9**, 2844 (2009).

[6] M. S. Nevius, M. Conrad, F. Wang, A. Celis, M. N. Nair, A. Taleb-Ibrahimi, A. Tejeda, and E. H. Conrad, Phys. Rev. Lett. **115**, 136802 (2015).

[7] M. N. Nair, I. Palacio, A. Celis, A. Zobelli, A. Gloter, S. Kubsky, J.-P. Turmaud, M. Conrad, C. Berger, W. de Heer,

E. H. Conrad, A. Taleb-Ibrahimi, and A. Tejeda, Nano Lett. **17**, 2681 (2017).
[8] I. Pletikosić, M. Kralj, P. Pervan, R. Brako, J. Coraux, A. T. N'Diaye, C. Busse, and T. Michely, Phys. Rev. Lett. **102**, 056808 (2009).
[9] P. Sutter, J. T. Sadowski, and E. Sutter, Phys. Rev. B **80**, 245411 (2009).
[10] T. Ohta, A. Bostwick, T. Seyller, K. Horn, and E. Rotenberg, Science **313**, 951 (2006).
[11] S. Y. Zhou, G.-H. Gweon, A. Fedorov, P. First, W. De Heer, D.-H. Lee, F. Guinea, A. C. Neto, and A. Lanzara, Nat. Mater. **6**, 770 (2007).
[12] A. Varykhalov, M. R. Scholz, T. K. Kim, and O. Rader, Phys. Rev. B **82**, 121101 (2010).
[13] C. Enderlein, Y. S. Kim, A. Bostwick, E. Rotenberg, and K. Horn, New J. Phys. **12**, 033014 (2010).
[14] C. Lin, X. Huang, F. Ke, C. Jin, N. Tong, X. Yin, L. Gan, X. Guo, R. Zhao, W. Yang, E. Wang, and Z. Hu, Phys. Rev. B **89**, 085416 (2014).
[15] M. Pisarra, D. Pacilé, P. Moras, P. M. Sheverdyaeva, A. Sindona, M. Papagno, and C. Carbone, Phys. Rev. B **89**, 195438 (2014).
[16] I. Šrut Rakić, M. Kralj, W. Jolie, P. Lazić, W. Sun, J. Avila, M.-C. Asensio, F. Craes, V. M. Trontl, C. Busse, and P. Pervan, Carbon **110**, 267 (2016).
[17] A. Celis, M. N. Nair, M. Sicot, F. Nicolas, S. Kubsky, D. Malterre, A. Taleb-Ibrahimi, and A. Tejeda, Phys. Rev. B **97**, 195410 (2018).
[18] K. Nakatsuji, Y. Shibata, R. Niikura, F. Komori, K. Morita, and S. Tanaka, Phys. Rev. B **82**, 045428 (2010).
[19] R. Balog, B. Jørgensen, L. Nilsson, M. Andersen, E. Rienks, M. Bianchi, M. Fanetti, E. Lægsgaard, A. Baraldi, S. Lizzit, Z. Sljivancanin, F. Besenbacher, B. Hammer, T. G. Pedersen, P. Hofmann, and L. Hornekær, Nat. Mater. **9**, 315 (2010).
[20] S. Niyogi, E. Bekyarova, M. E. Itkis, H. Zhang, K. Shepperd, J. Hicks, M. Sprinkle, C. Berger, C. N. Lau, W. A. deHeer, E. H. Conrad, and R. C. Haddon, Nano Lett. **10**, 4061 (2010).
[21] S. Rusponi, M. Papagno, P. Moras, S. Vlaic, M. Etzkorn, P. M. Sheverdyaeva, D. Pacilé, H. Brune, and C. Carbone, Phys. Rev. Lett. **105**, 246803 (2010).
[22] K. Kanetani, K. Sugawara, T. Sato, R. Shimizu, K. Iwaya, T. Hitosugi, and T. Takahashi, Proc. Natl. Acad. Sci. USA **109**, 19610 (2012).
[23] S. Ichinokura, K. Sugawara, A. Takayama, T. Takahashi, and S. Hasegawa, ACS Nano **10**, 2761 (2016).
[24] B. M. Ludbrook, G. Levy, P. Nigge, M. Zonno, M. Schneider, D. J. Dvorak, C. N. Veenstra, S. Zhdanovich, D. Wong, P. Dosanjh, C. Strasser, A. Stohr, S. Forti, C. R. Ast, U. Starke, and A. Damascelli, Proc. Natl. Acad. Sci. USA **112**, 11795 (2015).
[25] A. Luican, G. Li, A. Reina, J. Kong, R. R. Nair, K. S. Novoselov, A. K. Geim, and E. Y. Andrei, Phys. Rev. Lett. **106**, 126802 (2011).
[26] M. Yankowitz, J. Xue, D. Cormode, J. D. Sanchez-Yamagishi, K. Watanabe, T. Taniguchi, P. Jarillo-Herrero, P. Jacquod, and B. J. LeRoy, Nat. Phys. **8**, 382 (2012).
[27] D. Pierucci, H. Henck, J. Avila, A. Balan, C. H. Naylor, G. Patriarche, Y. J. Dappe, M. G. Silly, F. Sirotti, A. T. C. Johnson, M. C. Asensio, and A. Ouerghi, Nano Lett. **16**, 4054 (2016).
[28] H. C. Diaz, J. Avila, C. Y. Chen, R. Addou, M. C. Asensio, and M. Batzill, Nano Lett. **15**, 1135 (2015).
[29] W. Jin, P.-C. Yeh, N. Zaki, D. Chenet, G. Arefe, Y. Hao, A. Sala, T. O. Mentes, J. I. Dadap, A. Locatelli, J. Hone, and R. M. Osgood, Jr., Phys. Rev. B **92**, 201409(R) (2015).
[30] C.-H. Park, L. Yang, Y.-W. Son, M. L. Cohen, and S. G. Louie, Nat. Phys. **4**, 213 (2008).
[31] J. M. B. Lopes dos Santos, N. M. R. Peres, and A. H. Castro Neto, Phys. Rev. Lett. **99**, 256802 (2007).
[32] R. Bistritzer and A. H. MacDonald, Proc. Natl. Acad. Sci. USA **108**, 12233 (2011).
[33] H. Nishi, Y.-i. Matsushita, and A. Oshiyama, Phys. Rev. B **95**, 085420 (2017).
[34] E. Starodub, A. Bostwick, L. Moreschini, S. Nie, F. E. Gabaly, K. F. McCarty, and E. Rotenberg, Phys. Rev. B **83**, 125428 (2011).
[35] R. Larciprete, S. Ulstrup, P. Lacovig, M. Dalmiglio, M. Bianchi, F. Mazzola, L. Hornekær, F. Orlando, A. Baraldi, P. Hofmann, and S. Lizzit, ACS Nano **6**, 9551 (2012).
[36] S. Ulstrup, M. Andersen, M. Bianchi, L. Barreto, B. Hammer, L. Hornekær, and P. Hofmann, 2D Mater. **1**, 025002 (2014).
[37] L. A. Ponomarenko, R. V. Gorbachev, G. L. Yu, D. C. Elias, R. Jalil, A. A. Patel, A. Mishchenko, A. S. Mayorov, C. R. Woods, J. R. Wallbank, M. Mucha-Kruczynski, B. A. Piot, M. Potemski, I. V. Grigorieva, K. S. Novoselov, F. Guinea, V. I. Fal'ko, and A. K. Geim, Nature (London) **497**, 594 (2013).
[38] C. R. Dean, L. Wang, P. Maher, C. Forsythe, F. Ghahari, Y. Gao, J. Katoch, M. Ishigami, P. Moon, M. Koshino, T. Taniguchi, K. Watanabe, K. L. Shepard, J. Hone, and P. Kim, Nature (London) **497**, 598 (2013).
[39] W. Eberhardt, I. T. McGovern, E. W. Plummer, and J. E. Fischer, Phys. Rev. Lett. **44**, 200 (1980).
[40] M. Petrović, I. Šrut Rakić, S. Runte, C. Busse, J. T. Sadowski, P. Lazić, I. Pletikosić, Z. H. Pan, M. Milun, P. Pervan, N. Atodiresei, R. Brako, D. Šokčević, T. Valla, T. Michely, and M. Kralj, Nat. Commun. **4**, 2772 (2013).
[41] W. Jolie, F. Craes, M. Petrović, N. Atodiresei, V. Caciuc, S. Blügel, M. Kralj, T. Michely, and C. Busse, Phys. Rev. B **89**, 155435 (2014).
[42] Y. Lin, Surface Electron Dynamics for Intercalated Graphene (and Other 2D Materials) on a Metal Template, Ph.D. Thesis, Columbia University, 2019.
[43] G. Kresse and J. Furthmüller, Phys. Rev. B **54**, 11169 (1996).
[44] G. Kresse and D. Joubert, Phys. Rev. B **59**, 1758 (1999).
[45] P. E. Blöchl, Phys. Rev. B **50**, 17953 (1994).
[46] M. Dion, H. Rydberg, E. Schröder, D. C. Langreth, and B. I. Lundqvist, Phys. Rev. Lett. **92**, 246401 (2004).
[47] J. Klimeš, D. R. Bowler, and A. Michaelides, Phys. Rev. B **83**, 195131 (2011).
[48] Y. Xu and M. Mavrikakis, J. Chem. Phys. **116**, 10846 (2002).
[49] H. Zhang, A. Soon, B. Delley, and C. Stampfl, Phys. Rev. B **78**, 045436 (2008).
[50] J. Neugebauer and M. Scheffler, Phys. Rev. B **46**, 16067 (1992).
[51] J. P. Perdew, K. Burke, and M. Ernzerhof, Phys. Rev. Lett. **77**, 3865 (1996).
[52] C. Heske, R. Treusch, F. J. Himpsel, S. Kakar, L. J. Terminello, H. J. Weyer, and E. L. Shirley, Phys. Rev. B **59**, 4680 (1999).
[53] P. E. Trevisanutto, C. Giorgetti, L. Reining, M. Ladisa, and V. Olevano, Phys. Rev. Lett. **101**, 226405 (2008).

[54] W. Ku, T. Berlijn, and C.-C. Lee, Phys. Rev. Lett. **104**, 216401 (2010).
[55] V. Popescu and A. Zunger, Phys. Rev. Lett. **104**, 236403 (2010).
[56] V. Popescu and A. Zunger, Phys. Rev. B **85**, 085201 (2012).
[57] P. V. C. Medeiros, S. Stafström, and J. Björk, Phys. Rev. B **89**, 041407(R) (2014).
[58] P. V. C. Medeiros, S. S. Tsirkin, S. Stafström, and J. Björk, Phys. Rev. B **91**, 041116 (2015).
[59] N. Armbrust, J. Güdde, P. Jakob, and U. Höfer, Phys. Rev. Lett. **108**, 056801 (2012).
[60] K. Takahashi, M. Imamura, I. Yamamoto, J. Azuma, and M. Kamada, Phys. Rev. B **89**, 155303 (2014).
[61] D. Niesner and T. Fauster, J. Phys.: Condens. Matter **26**, 393001 (2014).
[62] S. Tan, A. Argondizzo, C. Wang, X. Cui, and H. Petek, Phys. Rev. X **7**, 011004 (2017).
[63] Y. Lin, Y. Li, J. T. Sadowski, W. Jin, J. I. Dadap, M. S. Hybertsen, and R. M. Osgood, Jr., Phys. Rev. B **97**, 165413 (2018).
[64] D. Niesner, T. Fauster, J. I. Dadap, N. Zaki, K. R. Knox, P.-C. Yeh, R. Bhandari, R. M. Osgood, Jr., M. Petrović, and M. Kralj, Phys. Rev. B **85**, 081402 (2012).
[65] S. Pagliara, M. Montagnese, S. Dal Conte, G. Galimberti, G. Ferrini, and F. Parmigiani, Phys. Rev. B **87**, 045427 (2013).
[66] S. Pagliara, S. Tognolini, L. Bignardi, G. Galimberti, S. Achilli, M. I. Trioni, W. F. van Dorp, V. Ocelík, P. Rudolf, and F. Parmigiani, Phys. Rev. B **91**, 195440 (2015).
[67] C. Busse, P. Lazić, R. Djemour, J. Coraux, T. Gerber, N. Atodiresei, V. Caciuc, R. Brako, A. T. N'Diaye, S. Blügel, J. Zegenhagen, and T. Michely, Phys. Rev. Lett. **107**, 036101 (2011).
[68] M. Kralj, I. Pletikosić, M. Petrović, P. Pervan, M. Milun, A. T. N'Diaye, C. Busse, T. Michely, J. Fujii, and I. Vobornik, Phys. Rev. B **84**, 075427 (2011).
[69] A. Varykhalov, D. Marchenko, M. R. Scholz, E. D. L. Rienks, T. K. Kim, G. Bihlmayer, J. Sánchez-Barriga, and O. Rader, Phys. Rev. Lett. **108**, 066804 (2012).
[70] J. Lehmann, M. Merschdorf, A. Thon, S. Voll, and W. Pfeiffer, Phys. Rev. B **60**, 17037 (1999).
[71] K. Takahashi, J. Azuma, and M. Kamada, Phys. Rev. B **85**, 075325 (2012).
[72] A. R. Law, M. T. Johnson, and H. P. Hughes, Phys. Rev. B **34**, 4289 (1986).
[73] S. Y. Zhou, G.-H. Gweon, C. D. Spataru, J. Graf, D.-H. Lee, S. G. Louie, and A. Lanzara, Phys. Rev. B **71**, 161403(R) (2005).
[74] I. Schäfer, M. Schlüter, and M. Skibowski, Phys. Rev. B **35**, 7663 (1987).
[75] R. Claessen, H. Carstensen, and M. Skibowski, Phys. Rev. B **38**, 12582 (1988).
[76] Y. B. Zhang, V. W. Brar, F. Wang, C. Girit, Y. Yayon, M. Panlasigui, A. Zettl, and M. F. Crommie, Nat. Phys. **4**, 627 (2008).
[77] Y. Liu, L. Zhang, M. K. Brinkley, G. Bian, T. Miller, and T. C. Chiang, Phys. Rev. Lett. **105**, 136804 (2010).
[78] P. Ayria, S.-i. Tanaka, A. R. T. Nugraha, M. S. Dresselhaus, and R. Saito, Phys. Rev. B **94**, 075429 (2016).
[79] T. O. Wehling, I. Grigorenko, A. I. Lichtenstein, and A. V. Balatsky, Phys. Rev. Lett. **101**, 216803 (2008).
[80] S. Tognolini, S. Achilli, L. Longetti, E. Fava, C. Mariani, M. I. Trioni, and S. Pagliara, Phys. Rev. Lett. **115**, 046801 (2015).